ACS APPLIED ENERGY MATERIALS
Cite This: ACS Appl. Energy Mater. XXXX, XXX, XXX−XXX
Article
www.acsaem.org

Addition of Monovalent Silver Cations to $CH_3NH_3PbBr_3$ Produces Crystallographically Oriented Perovskite Thin Films

Timothy D. Siegler,[†,‡] Yangning Zhang,[†,‡] Andrei Dolocan,[‡] Lauren C. Reimnitz,[†,‡] Aida Torabi,[∥] Michael K. Abney,[†,‡] Junho Choi,[§] Gabriel Cossio,[⊥] Daniel W. Houck,[†,‡] Edward T. Yu,[‡,⊥] Xiaoqin Li,[‡,§] Taylor B. Harvey,[∥] Delia J. Milliron,[†,‡] and Brian A. Korgel*[,†,‡]

[†]McKetta Department of Chemical Engineering, [‡]Texas Materials Institute, and [§]Department of Physics, Complex Quantum Systems, The University of Texas at Austin, Austin, Texas 78712-1062, United States

[∥]Department of Science and Mathematics, Texas A&M University-Central Texas, Killeen, Texas 76549, United States

[⊥]Microelectronics Research Center, Department of Electrical and Computer Engineering, The University of Texas at Austin, Austin, Texas 78758, United States

Supporting Information

ABSTRACT: The incorporation of monovalent silver (Ag^+) cations into methylammonium lead bromide ($CH_3NH_3PbBr_3$) perovskite films leads to a strongly preferred (001) crystallographic orientation on a wide variety of substrates, ranging from glass to mesoporous TiO_2. $CH_3NH_3PbBr_3$ films deposited without Ag^+ exhibit only a weakly preferred (011) orientation. Compositional maps and depth profiles from time-of-flight secondary ion mass spectrometry (TOF-SIMS) reveal Ag^+ segregated to grain boundaries and interfaces. In photovoltaic devices (PVs), addition of Ag^+ to MAPBr films resulted in poorer device performance, most likely because of the observed Ag^+ segregation in the films.

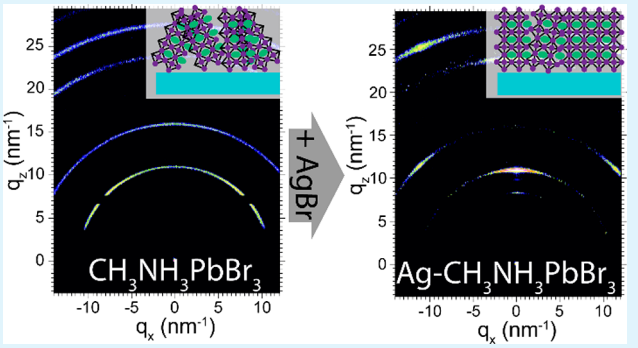

KEYWORDS: *perovskite, methylammonium lead bromide (MAPBr), crystallographic texture, silver doping, surface segregation, perovskite photovoltaics, photoluminescence*

INTRODUCTION

Methylammonium lead bromide ($CH_3NH_3PbBr_3$, MAPBr) is a lead halide perovskite with a wide band gap (2.3 eV).[1] It can be deposited on substrates from solution to fabricate a variety of optoelectronic devices, including light-emitting diodes (LEDs), photodetectors, and photovoltaics (PVs).[2−4] The crystallographic orientation, or texture, of the films is often important, and device performance has been improved by using crystallographically oriented perovskite films.[5−11] The charge carrier mobility, photoconductivity, trap state density, and degradation rates all depend on the crystal orientation of the film.[8,12−14] Recently, the addition of Ag^+ to methylammonium lead iodide ($CH_3NH_3PbI_3$, MAPI) has generated crystallographically oriented films.[5] In that case, there was also a "dedoping" effect that enhanced PV performance.[5] In this article, we show that the inclusion of Ag^+ in wider band gap MAPBr leads to (001)-oriented films on a wide variety of substrates but does not improve PV performance.

The crystallographic orientation of other perovskites has also been manipulated. In Ruddleston−Popper phases, where optoelectronic performance is strongly correlated to the orientation of the 2D inorganic layers with respect to the substrate, crystal orientation has been manipulated by either increasing the number of 3D layers between organic spacer ions,[15] controlling the annealing process,[16] or changing precursor stoichiometry.[10,17] Crystal texture has been controlled by arresting crystal nucleation with chlorine or acetate salts,[6,8,18,19] recrystallization in methylamine vapor,[6,7,20] alloying or ion exchange,[2,21−23] adjusting precursor stoichiometry,[13,24−26] seeding with nanoparticles,[27] or vapor phase epitaxy (VPE) on single crystal substrates of $SrTiO_3$ or NaCl.[28,29] Our method of inducing (001) crystal orientation involves the simple addition of Ag^+ to the precursor solution and does not appreciably impact thermal processing time or temperature. Additionally, it does not require the use of the expensive, atomically smooth single crystals needed for VPE.

EXPERIMENTAL SECTION

Materials. Lead bromide (>99.999% (metals basis) Puratonic, Alfa Aesar), silver bromide (99.998% (metals basis) Premion, Alfa Aesar), methylammonium bromide (CH_3NH_3Br, Greatcell Solar), dimethylformamide ($HCON(CH_3)_2$, 99.8%, anhydrous, Sigma), dimethyl sulfoxide ($(CH_3)_2SO$, ≥99.9%, anhydrous, Sigma), chlorobenzene (C_6H_5Cl, 99.8%, anhydrous, Sigma), zinc purum powder

Received: July 2, 2019
Accepted: July 12, 2019
Published: July 12, 2019

DOI: 10.1021/acsaem.9b01298
ACS Appl. Energy Mater. XXXX, XXX, XXX−XXX

(99%, Sigma), hydrochloric acid (Reagent grade, 37%, Fisher Chemical), titanium diisopropoxide bis(acetylacetanoate) (TAA, $C_{16}H_{32}O_6Ti$, 75 wt % in isopropanol, Sigma), 1-butanol (C_4H_9OH, 99.8%, anhydrous, Sigma), 30 NR-D nanoparticulate titanium dioxide paste (TiO_2, Greatcell Solar), ethanol (200 proof, Fisher Chemical), spiro-OMeTAD ((*N*²,*N*²,*N*²′,*N*²′,*N*⁷,*N*⁷,*N*⁷′,*N*⁷′-octakis(4-methoxyphenyl)-9,9′-spirobi[9*H*-fluorene]-2,2′,7,7′-tetramine, Merck), lithium bis(trifluoromethane)sulfonimide (LiTFSI, $LiC_2F_6NO_4S_2$, 99.95%, Sigma), acetonitrile (C_2H_3N, 99.8%, anhydrous, Sigma), 4-*tert*-butylpyridine ($C_9H_{13}N$, 96%, Sigma), and titanium tetrachloride ($TiCl_4$, 99.9%, Sigma) were used as received without further purification. Gold for evaporation (99.99%, 0.5 mm diameter wire) was purchased from Kurt J. Lesker.

Silicon substrates (University Wafer, 8−10 Ω·cm, polished (100) surface), tin-doped indium oxide (ITO)-coated glass (Thin Film Devices, 100 Ω/sq, >90% transparency), and fluorine-doped tin oxide (FTO)-coated glass (Hartford Glass) were used as received. Immediately prior to deposition of the perovskite films, substrates were rinsed with ethanol, placed in a Jelight Co. Inc. Model 42 UV-ozone cleaner for 1 h, and immediately transferred into a nitrogen-filled glovebox for perovskite deposition.

Deposition of $CH_3NH_3PbBr_3$ (MAPBr) Films. First, 514 mg of $PbBr_2$ and 157 of mg CH_3NH_3Br (MABr) were dissolved in 0.8 mL of DMF and 0.2 mL of DMSO by stirring for 2 h at room temperature to obtain reactant concentrations of 1.4 M of each $PbBr_2$ and MABr. In a separate vial, 263 mg of AgBr and 157 mg of MABr were dissolved in 0.8 mL of DMF and 0.2 mL of DMSO in a similar manner, resulting in solution concentrations of 1.4 M AgBr and MABr. (Note: we observed that AgBr does not dissolve in DMF/DMSO without the parallel dissolution of equimolar MABr.) The precursor solution was then prepared by mixing these AgBr and $PbBr_2$ solutions to achieve the desired Ag:Pb mole ratio (e.g., 1:9 AgBr:$PbBr_2$ for "10% Ag" samples) and deposited on the desired substrate by using a Laurel spin-coater in a nitrogen glovebox (<10 ppm of O_2, <10 ppm of H_2O). Films were spun by using a two-step program (1000 rpm for 10 s and 4000 rpm for 30 s) with 50 μL of precursor solution spread evenly across the substrate. After 15 s into the second step, 100 μL of chlorobenzene was pipetted onto the center of the substrate to induce crystallization of the film. The films were then annealed at 100 °C for 1 h on a hot plate in a nitrogen glovebox while continuously purging the box with nitrogen to avoid solvent vapor accumulation.

PV Device Fabrication and Testing. Photovoltaic devices (PVs) were fabricated by using established procedures in the literature.[30] FTO-coated glass was rinsed with dilute dish soap, DI water, and ethanol and then patterned by chemically etching the FTO from unwanted areas with zinc powder and concentrated hydrochloric acid. After the acid was neutralized with water, the patterned substrates were rinsed with DI water, sonicated in ethanol for 30 min, and treated with UV-ozone plasma for 1 h. A compact TiO_2 layer was deposited by mixing 72.5 μL of titanium diisopropoxide bis-(acetylacetanoate) in 1 mL of 1-butanol and then spin-coating this solution at 700 rpm for 10 s, 1000 rpm for 10 s, and 2000 rpm for 30 s. The film was dried by heating at 125 °C for 10 min, and then the 30 NR-D TiO_2 nanoparticulate paste dissolved at a concentration of 100 mg/mL in ethanol was deposited by using the same three-step spin-coating process used for TAA. The substrates were then heated at 550 °C for 1 h in air, which formed a mesoporous TiO_2 substrate. Immediately before solar cell fabrication, the TiO_2 films were immersed in aqueous 20 μM $TiCl_4$ for 10 min at 90 °C. The substrates were then rinsed with water and ethanol, cooled, and then annealed at 500 °C for 30 min in air. After the substrates were exposed to UV-ozone for 1 h, MAPBr was deposited by using the previously described spin-coating procedure. Spiro-OMeTAD was then deposited by spin-coating a solution of 72 mg/mL spiro-OMeTAD dissolved in 1 mL of chlorobenzene with 7.5 μL/mL of *tert*-butylpyridine and 24 μL/mL of lithium tetrafluorosulfonimide stock solution (170 mg of LiTFSI salt in 1 mL of acetonitrile) at 5000 rpm for 30 s. Spiro-coated MAPBr films were then left to sit overnight in a dry air desiccator before gold (~60 nm) was thermally evaporated at a rate of 2 Å/s and at a base pressure of 5×10^{-5} Torr.

PV device testing was performed by using light from a Xe lamp passed through an AM 1.5 filter with 100 mW cm^{-2} intensity, with intensity calibration performed on a Hamamatsu silicon diode. Current−voltage (*J*−*V*) profiles were obtained without light or voltage prebiasing by using a Keithley 2400 general purpose source meter swept at a constant rate of ~100 mV/s. External quantum efficiency (EQE) measurements were taken with a commercial solar cell spectral response measurement system (model QEX10, PV Measurements, Inc.) using a Xe arc lap source and a dual-grating monochromator with respective color filters. The EQE measurements were calibrated with a NIST certified silicon photodiode (SN: 98599).

Materials Characterization. Grazing incidence wide-angle X-ray scattering (GIWAXS) was performed on samples under vacuum by using a SAXSLAB Ganesha SAXS-WAXS system with monochromatic Cu Kα X-rays (λ = 1.54 Å) with a 5° incident beam angle. Scattered X-rays were captured for 10 min with a 487 × 619 pixel Pilatus3 R 300k (pixel size of 172 × 172 μm^2) detector and a sample-to-detector distance of 131 mm. Ewald sphere correction and linear integration (azimuth angle and 2θ) were processed with Fit2D software (version: 12_077_i686_WXP). Azimuth integration of the (001) peak was performed between q = 10.2 nm^{-1} and q = 11.6 nm^{-1} (14.3° to 16.4° 2θ) with 180 azimuth bins.

A Kratos Axis Ultra DLD X-ray photoelectron spectrometer (XPS) equipped with a monochromatic aluminum X-ray source was used to carry out X-ray photoelectron spectroscopy (XPS) measurements. Exposure of the samples to air was avoided by using a patented transfer system developed at the Texas Materials Institute (TMI) at the University of Texas at Austin.[31] Samples were loaded and sealed into the pressure-to-vacuum (P2V) transfer chamber in a nitrogen glovebox. The P2V chamber was then taken to the XPS instrument and evacuated before samples were transferred to the analysis chamber as described by Celio.[31] XPS data were analyzed by using CasaXPS software, correcting for sample charging by normalizing the C 1s signal from adventitious carbon to a binding energy of 284.8 eV. Peak fitting was performed by using Shirley, Tougaard, or Linear backgrounds, depending on the shape of the background in the specific region of fitting,[32] and a Gaussian−Lorentzian peak shape. Compositional data were obtained by integrating the peaks with corrected intensities based on the relative sensitivity factor provided by the Kratos library.

Time-of-flight secondary ion mass spectrometry (TOF-SIMS) data were acquired by using an ION-TOF GmbH 2010 TOF.SIMS 5 instrument with a pulsed Bi^+ analysis beam (20 ns pulse width, 30 keV ion energy, and ~3.5 pA measured sample current) and a O_2^+ sputtering beam (1 keV and 41.3 nA measured sample current current) at ~10^{-9} Torr base pressure. During depth profiling the analysis beam was raster-scanned over a 0.1 × 0.1 mm^2 area centered within the 0.3 × 0.3 mm^2 sputtered area of the sputtering beam. Analysis was performed in interlaced mode as described by Wang et al.[33] and in positive mode; i.e., all secondary ions detected were positively charged fragments. To alleviate electrical charging of the sample, an electron beam with a constant energy of 21 eV was directed at the sample during analysis. All depth profiles were acquired in high current bunched mode. For TOF-SIMS mapping with high lateral resolution, the analysis beam was set in the burst alignment mode using seven bursts. Before data acquisition, a very thin layer of sample was removed from the surface using 30 s of O_2^+ sputter. The O_2^+ sputtering rate was calculated to be ~0.2 nm s^{-1} based on the depth profile of the $InSnO^+$ secondary ion fragment and sample thickness from cross-section SEM. To avoid peak overlap of Ag^+ and $SiBr^+$ ion fragments, ITO-coated borosilicate glass was used as a substrate for TOF-SIMS measurements.

Scanning electron microscopy (SEM) and energy dispersive X-ray spectroscopy (EDS) data were obtained with a Hitachi S550 SEM/STEM operated at 30 kV and 10 μA with a Bruker AXS XFlash Detector 4010. The MAPBr films were spin-coated on silicon substrates (University Wafer, 8−10 Ω·cm, polished (100) surface).

DOI: 10.1021/acsaem.9b01298
ACS Appl. Energy Mater. XXXX, XXX, XXX−XXX

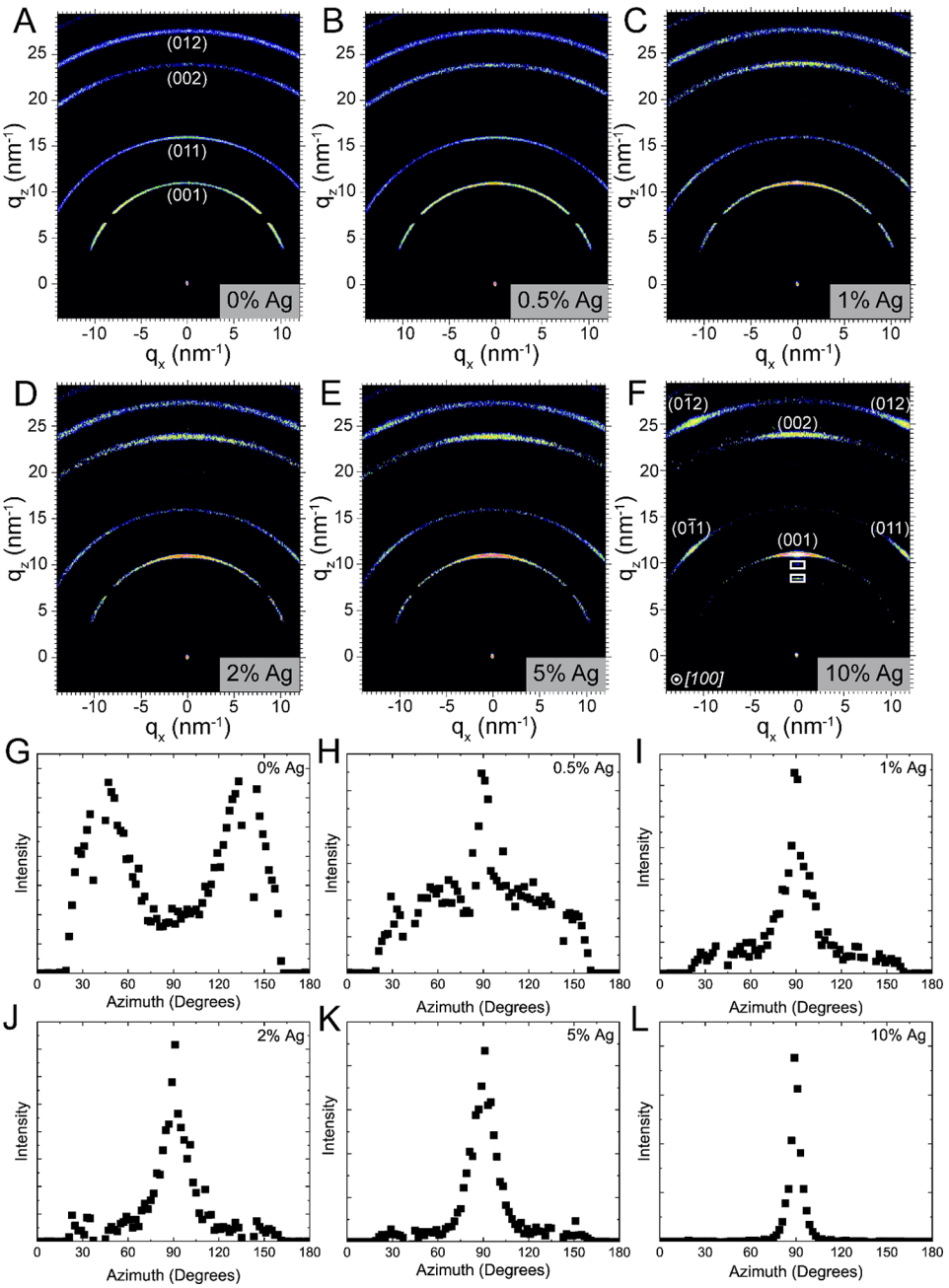

Figure 1. (A–F) GIWAXS of MAPBr films on silicon substrates with varying amounts of Ag^+. The Ag concentration corresponds to the molar percentage of Ag^+ added to the precursor solution with respect to $[Pb^{2+}]$. The indexing in (F) corresponds to cubic MAPBr (PDF #01-084-9476) with a [100] beam direction. Additional diffraction spots are observed in (F), which are enclosed in rectangles. (G–L) Diffraction intensity of the (001) ring ($10.3\ nm^{-1} < q < 11.6\ nm^{-1}$ or $14.3° < 2\theta < 16.4°$) from the GIWAXS patterns in (A–F) is plotted as a function of azimuthal angle ϕ. The (001) peaks at 45° and 135° in (G) indicate that MAPBr without added Ag^+ exhibits some preferential (011) orientation. Silver addition leads to a significant sharpening of the (001) signal at 90°, indicating that the film is oriented with (001) planes parallel to the substrate.

SEM images and compositional profiles of the cross-sectioned films were obtained by using a JEOL-7610F SEM equipped with a 1040 Oxford Instruments EDX detector.

Photoluminescence (PL) was measured on a Fluorolog-3 spectrophotometer (Horiba Jobin Yvon) using an excitation wavelength of 400 nm and a slit size of 5 for both excitation and emission. TRPL measurements were performed in a homemade time-correlated single photon counting (TCSPC) setup equipped with a picosecond pulse laser diode (fwhm = 100 ps, λ = 446 nm, repetition rate = 1 MHz). A 10× (0.28 numerical aperture) objective focused the light to the sample, and the same objective collected PL signal. The collected PL was directed through a band-pass filter, a spectrograph, and an avalanche photodiode (APD, SPCM-AQRH-14). The measured instrument response function was 600 ps, much lower than measured lifetimes.

RESULTS AND DISCUSSION

Figure 1 shows grazing incidence wide-angle X-ray scattering (GIWAXS) from MAPBr films deposited on silicon substrates by room temperature spin-coating with increasing amounts of AgBr in the precursor solution. Molar ratios of $[Ag^+]/[Pb^{2+}]$ ranged from 0.5% to 10%, and the films were annealed at 100 °C after deposition.[34] All patterns index to cubic MAPBr with a lattice constant of 5.92 Å. Substitutional replacement of Pb^{2+}

DOI: 10.1021/acsaem.9b01298
ACS Appl. Energy Mater. XXXX, XXX, XXX–XXX

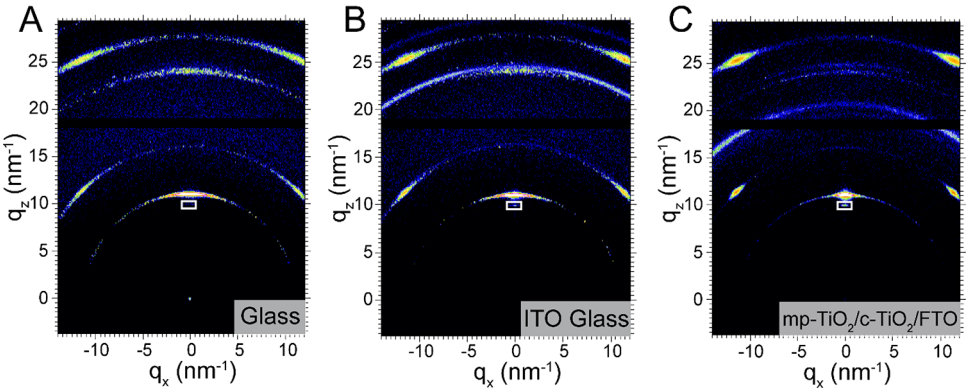

Figure 2. GIWAXS of MAPBr films deposited with 10 mol % Ag^+ in the precursor solution on (A) glass, (B) ITO-coated glass, and (C) FTO glass coated with a compact and mesoporous TiO_2 layer. The films exhibit a (001) crystal orientation. The diffraction spots outlined with rectangles correspond to an impurity phase. Additional GIWAXS data of MAPBr films on these substrates with different Ag^+ concentrations are provided as Supporting Information.

Table 1. Elemental Composition of MAPBr Films Determined by EDS[a] and XPS

	Ag/(Ag + Pb) (%)		Br:Pb		N:Pb
Ag (mol %) in soln	XPS	EDS	XPS	EDS	XPS
0	0	below LOD[a]	2.6 ± 0.2	3.1 ± 0.6	0.94 ± 0.14
0.5	3.2 ± 0.5	below LOD[a]	2.6 ± 0.2	3.0 ± 0.5	0.99 ± 0.13
1	8.2 ± 0.5	below LOD[a]	2.6 ± 0.3	3.2 ± 0.6	0.96 ± 0.12
2	8.8 ± 0.5	4 ± 7	2.7 ± 0.2	3.7 ± 1.4	1.1 ± 0.12
5	10.3 ± 0.6	12 ± 8	2.9 ± 0.2	3.3 ± 0.1	1.3 ± 0.14
10	8.7 ± 0.5	18 ± 9	2.9 ± 0.2	3.5 ± 0.3	1.5 ± 0.20

[a]The limit of detection (LOD) for EDS is ~3 at. %.

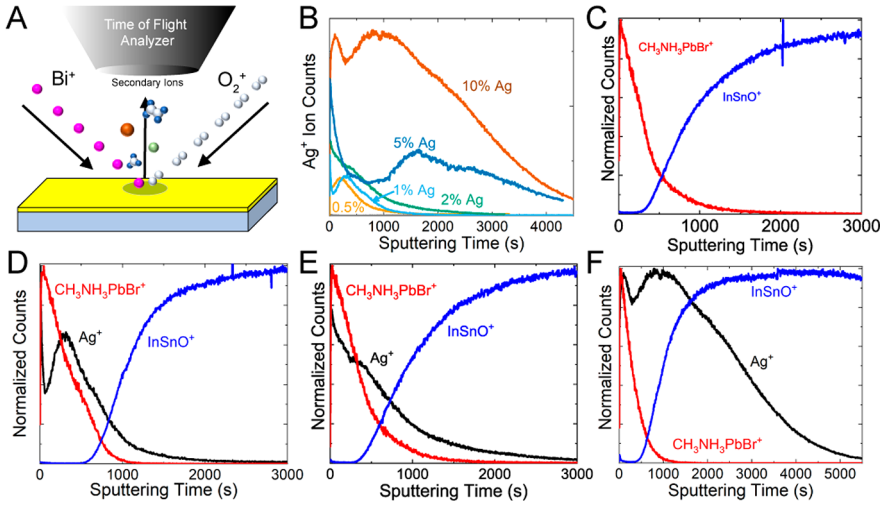

Figure 3. (A) Schematic of the TOF-SIMS measurement. (B) TOF-SIMS profiles of Ag secondary ion yield. (C–F) TOF-SIMS depth profiles of Ag, CH_3NH_3PbBr, and InSnO secondary ion fragments in MAPBr films deposited with (C) 0%, (D) 1%, (E) 2%, and (F) 10% Ag^+ in the precursor solution (see the Supporting Information for additional TOF-SIMS data).

with Ag^+ does not change the lattice constant because of similar ionic radii of Pb^{2+} (119 pm) and Ag^+ (115 pm).[35] This constant lattice parameter confirms that Ag^+ substitutes in the B-site and not the A-site, as MA^+ has an ionic radius of 248 pm.[36] When $[Ag^+]$:$[Pb^{2+}]$ ratios exceeded 2%, the GIWAXS data exhibited significant texture. In Figures 1D–F and 1J–L, the enhanced diffraction of the (001) and (011) rings at ϕ = 90° and ϕ = 45°, respectively, indicate that the films are predominantly oriented with (001) lattice planes parallel to the substrate. A faint texture is also present in the pure MAPBr films in Figures 1A,G, which corresponds to a different, weakly preferred (011) crystal orientation.

MAPBr films were also deposited on glass, ITO-coated glass, and FTO glass coated with mesoporous TiO_2. Figure 2 shows GIWAXS data for the films with 10% Ag^+. There is a significant amount of texture, and all of the patterns show a (001) crystallographic orientation. The same impurity features as in Figure 1F are also observed in these films with high Ag^+ concentration.

Compositional profiles were obtained by using X-ray photoelectron spectroscopy (XPS), energy-dispersive X-ray

DOI: 10.1021/acsaem.9b01298
ACS Appl. Energy Mater. XXXX, XXX, XXX–XXX

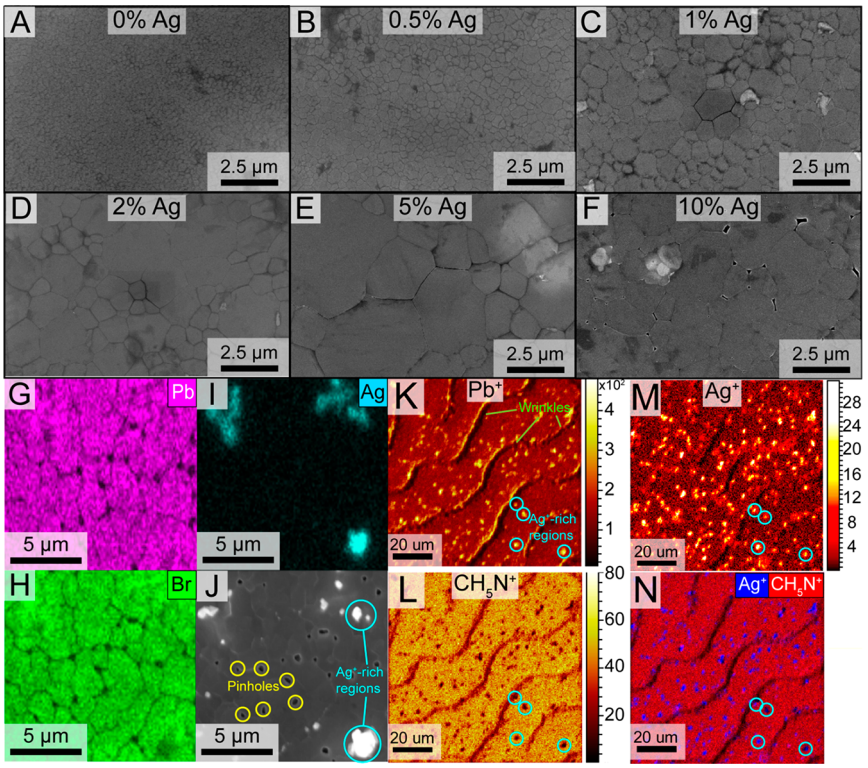

Figure 4. (A–F) Top-down SEM images of MAPBr films on silicon deposited with (A) 0%, (B) 0.5%, (C) 1%, (D) 2%, (E) 5%, and (F) 10% Ag^+ added to the precursor solution. The crystal grain size increases with increasing Ag^+, and pinholes are observed when the Ag^+ concentration reaches 10% Ag^+. (G–I) EDS maps of (G) Pb, (H) Br, and (I) Ag corresponding to the region imaged by SEM in (J) for a MAPBr film with 10% Ag^+. (K–N) TOF-SIMS mapping of a 2% Ag MAPBr thin film on ITO showing the (K) lead, (L) methylamine, (M) silver, and (N) an overlay of the Ag and CH_5N^+ signals. The wavelike features are due to thickness variations in the film.

spectroscopy (EDS), and time-of-flight secondary ion mass spectroscopy (TOF-SIMS). The XPS and EDS data are shown in Table 1. MAPBr films deposited without Ag^+ are stoichiometric. The addition of Ag^+ led to higher Br:Pb and N:Pb ratios, indicating that some unreacted CH_3NH_3Br is present. The silver concentrations measured by XPS are higher than those measured by EDS. XPS is surface-sensitive,[37,38] while EDS provides a spatially averaged composition. This means that Ag^+ accumulates at the interface. However, above 2% Ag^+, EDS and XPS analyses become more consistent, indicating this surface segregation may be more subtle or disappear for higher Ag^+ concentrations. To determine whether Ag^+ still accumulated at interfaces at higher concentrations, TOF-SIMS, a more sensitive elemental analysis, was used to map the composition in greater detail.

In TOF-SIMS, the concentrations of species in a film are determined as a function of depth by sputtering the layers and measuring the composition of the fragments, as illustrated in Figure 3A.[39] Figure 3B shows the Ag secondary ion yield, and Figures 3C–F show TOF-SIMS profiles of three secondary ion fragments from MAPBr films on ITO-coated glass substrates. In its absolute amount, the secondary ion yield of a given fragment is proportional to the concentration of the corresponding element/molecule in the film. These ion fragments were chosen due to their secondary ion yield and to what they correspond with in the film: Ag corresponds to silver, CH_3NH_3PbBr corresponds to MAPBr, and InSnO corresponds to the ITO substrate. The uniform background signal of the CH_3NH_3PbBr secondary ion yield is similar for all of the samples, whereas the Ag secondary ion yield increased with the amount of Ag^+ added to the film. The depth localization of the elements/molecules is inferred by normalizing the secondary ion yields to the maximum yield value of each species. The Ag concentration is highest at the top and bottom interfaces of the MAPBr film. There is also evidence of Ag penetration into the ITO layer.

The composition on the surface of the films was also mapped. Figures 4G–I show EDS maps of Pb, Br, and Ag in the region of the MAPBr film imaged by SEM in Figure 4J. There are features concentrated with Ag. Figures 4K–N show higher resolution compositional profiles obtained by TOF-SIMS. These maps show phase-segregated regions rich in Ag^+. The spatial distributions of Pb, CH_5N, and Ag secondary ions are relatively uniform, except for bright spots of Ag and wavelike features. The dark waves are shadows in the TOF-SIMS signal resulting from wrinkles or thickness undulations.[9,40,41] The maps of Pb and CH_5N secondary ion yields in Figures 4K,L indicate that the Ag^+-rich regions contain Pb^{2+}, but not $CH_3NH_3^+$. The absence of $CH_3NH_3^+$ in the Ag^+-rich regions is more apparent in the overlay of Ag and CH_5N secondary ion yield maps in Figure 4N. We propose that these domains composed of Ag, Pb, and Br are giving rise to the additional diffraction spots at low q in the GIWAXS patterns in Figures 1F and 2, although the diffraction spots did not match any known silver-containing compounds in the COD or ICDD diffraction databases. The difference in the extent of silver-rich domains observed in EDS analysis compared to a normal top-down SEM image seen in Figures 4I,J indicates that these AgPbBr domains are not exclusive to film sensitivities at higher Ag compositions. This explains converging EDS and XPS

DOI: 10.1021/acsaem.9b01298
ACS Appl. Energy Mater. XXXX, XXX, XXX–XXX

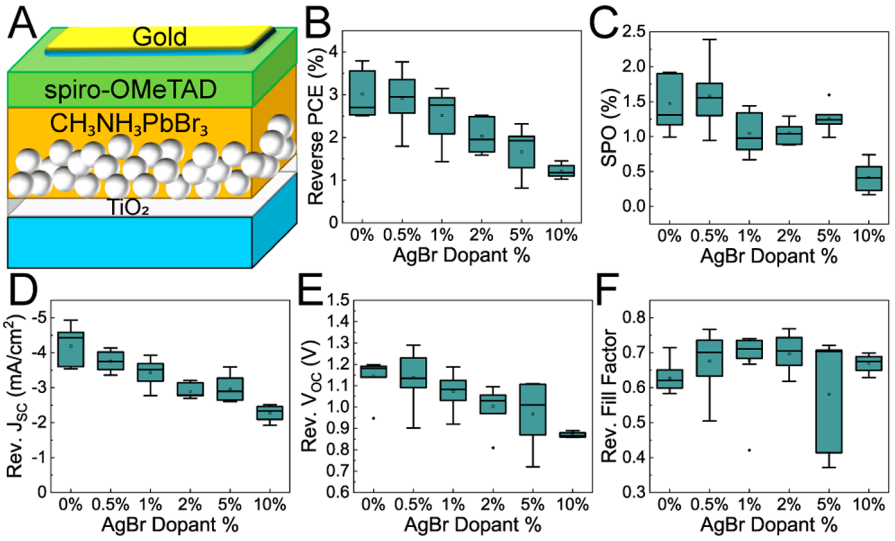

Figure 5. (A) PV device architecture and materials stack. (B–F) Histograms of (B) reverse scan PCE, (C) stabilized power output (SPO), (D) short-circuit current (J_{SC}) of the reverse scan, (E) open-circuit voltage (V_{OC}) of the reverse scan, and (F) fill factor of the reverse scan of MAPBr PVs with different amounts of AgBr added to the precursor solution (J–V device responses are provided as Supporting Information).

analysis in Table 1, as the convergence in measured Ag concentration between the two analyses correlates with the emergence of these secondary domains.

Photovoltaic devices (PVs) were fabricated with Ag^+-doped MAPBr films by using the materials stack in Figure 5A. As shown in Figures 5B–F, the addition of Ag^+ degraded device performance, decreasing the power conversion efficiency (PCE), stabilized power output (SPO), short-circuit current (J_{SC}), and open-circuit voltage (V_{OC}). This is not due to differences in film morphology, as the MAPBr films look similar in top-down SEM images (Figures 4A–F). In fact, films with more Ag^+ have larger crystal grain size and even smoother morphology—most likely due to the increased crystallographic orientation of the films. Films deposited with more than 10% Ag^+ in the deposition solution did form pinholes near grain boundaries, but the devices still functioned. The reduction in device performance became significant once the Ag^+ concentration exceeded 2%, corresponding to the point where the Ag–Pb–Br impurity emerged.

Photoluminescence (PL) measurements are taken on Ag^+-doped MAPBr films on UV-ozone-treated glass to determine the impact of silver doping on the luminescence behavior of thin films. Results are shown in Figure 6. The PL spectra and time-resolved photoluminescence (TRPL) decay do not change dramatically as a function of silver content, seen in Figures 6A and 6B, respectively. The only noticeable change is in the static PL spectra in Figure 6A, where the PL peak slightly blue-shifts and the shoulder in the long wavelength range noticeably decreases above 5% Ag^+ incorporation. PL peak intensity is similar from sample to sample, seen in Figure S9. The intensity goes up as a function of Ag content but correlates more closely with film thickness than with silver content. This red shoulder is observed in thick films and single crystals. It has been recently attributed to radiative recombination via indirect Rashba transitions.[42] Interestingly, in contrast to literature observations of Ag-free MAPBr, this red shoulder disappears as the film thickness increases (see the Supporting Information for cross-sectional SEM images).[42] TRPL data taken at 540 nm, however, do not exhibit systematic changes with increasing Ag^+ content, seen in Figure 6B. The 5% Ag samples appear to have shorter lifetimes, which may be due to the introduction of trap states in the material. Curves are fit to a biexponential function with the equation $I = A_1e^{-\tau_1} + A_2e^{-\tau_2}$ and the fitting parameters A_1, A_2, τ_1, and τ_2 are shown in Table 2. Fitting curves are shown in the Supporting Information. Calculated lifetimes in Table 2 are slightly shorter

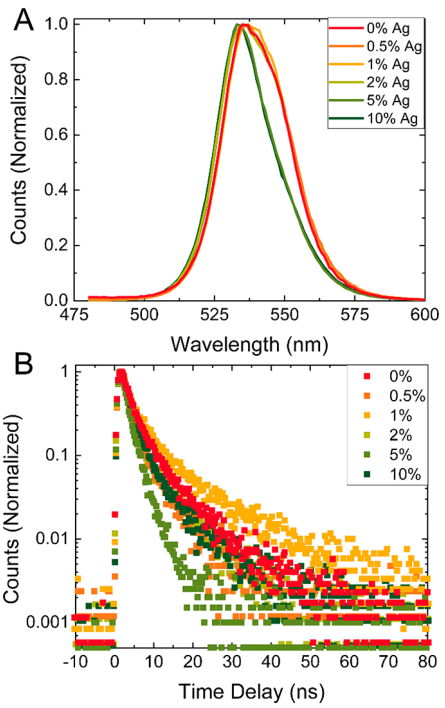

Figure 6. (A) Steady-state PL spectra and (B) TRPL decay at 540 nm for Ag^+-doped MAPBr thin films. PL was excited at 400 nm and TRPL data at 446 nm. Above 5% Ag^+ incorporation, a subtle blue-shift in the PL peak is observed, and the red shoulder of the MAPBr PL spectra reduces in intensity. No systematic trend in PL lifetime is observed in (B), with the exception of the 5% Ag^+ film, which has a shorter lifetime, likely due to trap states introduced with the introduction of Ag^+.

DOI: 10.1021/acsaem.9b01298
ACS Appl. Energy Mater. XXXX, XXX, XXX–XXX

Table 2. Fitting Parameters for Biexponential Fits of the PL Decay at 540 nm (Plots of Fits Are Provided as Supporting Information)

Ag (mol %) in soln	A_1	τ_1 (ns)	A_2	τ_2 (ns)
0	0.87	2.87	0.13	10.9
0.5	0.84	1.92	0.16	7.23
1	0.77	2.60	0.23	12.2
2	0.88	1.89	0.12	9.60
5	0.99	2.06	0.0090	15.5
10	0.94	2.65	0.059	13.8

yet overall consistent with other reports of PL lifetime in the literature.[42]

Others have also reported on the effects of silver in perovskite optoelectronics. Silver doping has improved some devices[43−45] and increased the mobility of hybrid organic−inorganic perovskite (HOIP) nanoparticle films.[46] Yet, it has also degraded device performance when present in the form of silver halide as a product of corrosion.[47−51] Surface segregation of Ag^+ can negatively impact the depletion region, increase surface recombination, and lead to unwanted band offsets in the MAPBr film.[52−54] Unreacted CH_3NH_3Br can also harm PV performance.[47−49,55−57]

On the basis of the TOF-SIMS results and the compositional maps, we propose that segregation of Ag^+ to the interfaces of the MAPBr film—or "surface doping"—templates the (001) crystallographic orientation. This surface doping mechanism is illustrated in Figure 7. This mechanism is different than what occurs in MAPI films. In oriented MAPI films, the addition of Ag^+ significantly slows the crystallization rate, affecting nucleation and growth and ultimately the orientation of the film. In the case of MAPBr, there is no observed slowing of crystallization when Ag^+ is added. This is because the solvent−antisolvent spin-coating process used here induces crystallization within a few seconds of antisolvent exposure and does not depend on precursor composition.[34] Anisotropy in the interfacial energy of crystal surfaces tends to orient crystallizing grains to minimize surface energy in a film,[58−61] and the interfacial energies of crystal planes can be significantly modified by impurities or the adsorption of small molecules.[22,23,62−64] Silver(I) has been shown to be particularly active in this role in a wide variety of different instances, ranging from superconductor materials like $(Bi,Pb)_2Sr_2Ca_2Cu_3O_x$[65,66] and Y_2BaCuO_5[67] to plasmonic gold nanocrystals and nanorods.[68,69] High concentrations of Ag at the back interface of the MAPBr films observed in the TOF-SIMS profiles might lower the (001) surface energy, or MAPBr crystallization could be initiating at the liquid−air interface and proceeding toward the substrate, as in the "oriented crust" crystallization mechanism,[17,70] with Ag^+ templating (001)-oriented growth at the liquid−air interface. Either of these mechanisms would explain why the crystallographic orientation was not affected by the substrate.

In summary, we have identified a mechanism of Ag^+ surface doping that produces crystallographically oriented MAPBr films. Silver preferentially segregates to grain boundaries and interfaces and induces a preferred orientation of (001) MAPBr crystal planes parallel to the substrate. Although the PV performance did not improve with Ag^+ addition—most likely due to the formation of a separate phase composed of silver, lead and bromide—this report demonstrates more broadly that surface segregation of dopants can change the crystallographic orientation of a perovskite film.

■ ASSOCIATED CONTENT

Supporting Information

The Supporting Information is available free of charge on the ACS Publications website at DOI: 10.1021/acsaem.9b01298.

GIWAXS from MAPBr films with Ag^+ on different substrates, additional TOF-SIMS depth profiles, $J-V$ and incident photon-to-current efficiency (IPCE) data from MAPBr PV devices, integrated GIWAXS pattern showing the secondary phase diffraction peaks, SEM of cross-sectioned films, TRPL fits, and non-normalized PL spectra (PDF)

■ AUTHOR INFORMATION

Corresponding Author

*E-mail: korgel@che.utexas.edu.

ORCID

Timothy D. Siegler: 0000-0001-6033-2232
Yangning Zhang: 0000-0001-5511-955X
Andrei Dolocan: 0000-0001-5653-0439
Delia J. Milliron: 0000-0002-8737-451X
Brian A. Korgel: 0000-0001-6242-7526

Notes

The authors declare no competing financial interest.

■ ACKNOWLEDGMENTS

The authors acknowledge financial support of this work from the Robert A. Welch Foundation (F-1464, F-1662, F-1848), the NSF Industry/University Cooperative Research Center on Next Generation Photovoltaics (IIP-1540028, IIP-1624539, IIP-1822206), The Center for Dynamics and Control of Materials (CDCM) Materials Research Science and Engineering Center (MRSEC) supported by the NSF (DMR-1720595), and NSF Grants DMR-0923096, CBET-1702944, and CBET-1624659. T.D.S. acknowledges support by the United States

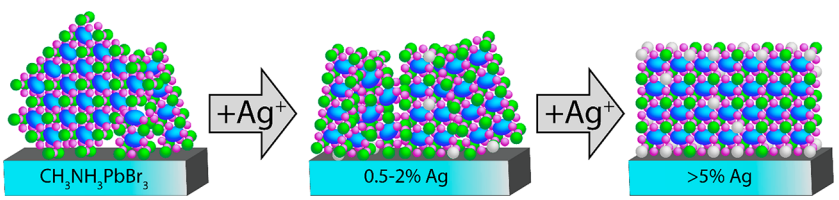

Figure 7. Illustration of an Ag^+ cation surface doping mechanism that induces crystallographic orientation of MAPBr films. Blue spheres represent methylammonium, green are lead, purple are bromide, and gray are silver atoms. MAPBr exhibits a weakly favored (011) orientation on the substrate. The addition of Ag^+ at low concentrations (0.5−2% Ag^+) leads to a weakly preferred (001) orientation, and higher Ag^+ concentrations (>5% Ag^+) lead to a strongly preferred (001) crystal orientation.

DOI: 10.1021/acsaem.9b01298
ACS Appl. Energy Mater. XXXX, XXX, XXX−XXX

Government under DoD, Air Force Office of Scientific Research, National Defense Science and Engineering Graduate (NDSEG) Fellowship, 32 CFR 168a. We thank Hugo Celio for assistance with XPS.

REFERENCES

(1) Park, J.-S.; Choi, S.; Yan, Y.; Yang, Y.; Luther, J. M.; Wei, S.-H.; Parilla, P.; Zhu, K. Electronic Structure and Optical Properties of α-$CH_3NH_3PbBr_3$ Perovskite Single Crystal. *J. Phys. Chem. Lett.* **2015**, *6*, 4304−4308.

(2) Kojima, A.; Teshima, K.; Shirai, Y.; Miyasaka, T. Organometal Halide Perovskites as Visible-Light Sensitizers for Photovoltaic Cells. *J. Am. Chem. Soc.* **2009**, *131*, 6050−6051.

(3) Heo, J. H.; Song, D. E.; Im, S. H. Planar $CH_3NH_3PbBr_3$ Hybrid Solar Cells with 10.4% Power Conversion Efficiency, Fabricated by Controlled Crystallization in the Spin-Coating Process. *Adv. Mater.* **2014**, *26*, 8179−8183.

(4) Lee, S.; Park, J. H.; Nam, Y. S.; Lee, B. R.; Zhao, B.; Di Nuzzo, D.; Jung, E. D.; Jeon, H.; Kim, J.-Y.; Jeong, H. Y.; Friend, R. H.; Song, M. H. Growth of Nano-Sized Single Crystals for Efficient Perovskite Light-Emitting Diodes. *ACS Nano* **2018**, *12*, 3417−3423.

(5) Abdi-Jalebi, M.; Pazoki, M.; Philippe, B.; Dar, M. I.; Alsari, M.; Sadhanala, A.; Divitini, G.; Imani, R.; Lilliu, S.; Kullgren, J.; Rensmo, H.; Grätzel, M.; Friend, R. H. Dedoping of Lead Halide Perovskites Incorporating Monovalent Cations. *ACS Nano* **2018**, *12*, 7301−7311.

(6) Dou, B.; Whitaker, J. B.; Bruening, K.; Moore, D. T.; Wheeler, L. M.; Ryter, J.; Breslin, N. J.; Berry, J. J.; Garner, S. M.; Barnes, F. S.; Shaheen, S. E.; Tassone, C. J.; Zhu, K.; van Hest, M. F. A. M. Roll-to-Roll Printing of Perovskite Solar Cells. *ACS Energy Lett.* **2018**, *3*, 2558−2565.

(7) Foley, B. J.; Cuthriell, S.; Yazdi, S.; Chen, A. Z.; Guthrie, S. M.; Deng, X.; Giri, G.; Lee, S.-H.; Xiao, K.; Doughty, B.; Ma, Y.-Z.; Choi, J. J. Impact of Crystallographic Orientation Disorders on Electronic Heterogeneities in Metal Halide Perovskite Thin Films. *Nano Lett.* **2018**, *18*, 6271−6278.

(8) Kim, D. H.; Park, J.; Li, Z.; Yang, M.; Park, J.-S.; Park, I. J.; Kim, J. Y.; Berry, J. J.; Rumbles, G.; Zhu, K. 300% Enhancement of Carrier Mobility in Uniaxial-Oriented Perovskite Films Formed by Topotactic-Oriented Attachment. *Adv. Mater.* **2017**, *29*, 1606831.

(9) Li, M.; Wang, Z.-K.; Zhuo, M.-P.; Hu, Y.; Hu, K.-H.; Ye, Q.-Q.; Jain, S. M.; Yang, Y.-G.; Gao, X.-Y.; Liao, L.-S. Pb-Sn-Cu Ternary Organometallic Halide Perovskite Solar Cells. *Adv. Mater.* **2018**, *30*, 1800258.

(10) Li, M.-H.; Yeh, H.-H.; Chiang, Y.-H.; Jeng, U.-S.; Su, C.-J.; Shiu, H.-W.; Hsu, Y.-J.; Kosugi, N.; Ohigashi, T.; Chen, Y.-A.; Shen, P.-S.; Chen, P.; Guo, T.-F. Highly Efficient 2D/3D Hybrid Perovskite Solar Cells via Low-Pressure Vapor-Assisted Solution Process. *Adv. Mater.* **2018**, *30*, 1801401.

(11) Ji, L.; Hsu, H.-Y.; Lee, J. C.; Bard, A. J.; Yu, E. T. Solution-Processed Epitaxial Growth of Hybrid Halide Perovskites and High-Performance Photodetectors. *Nano Lett.* **2018**, *18*, 994−1000.

(12) Jing, L.; Cheng, X.; Yuan, Y.; Du, S.; Ding, J.; Sun, H.; Zhan, X.; Zhou, T.-L. Design Growth of Triangular Pyramid $MAPBr_3$ Single Crystal and its Photoelectric Anisotropy between (100) and (111) Facets. *J. Phys. Chem. C* **2019**, *123*, 10826−10830.

(13) Zheng, G.; Zhu, C.; Ma, J.; Zhang, X.; Tang, G.; Li, R.; Chen, Y.; Li, L.; Hu, J.; Hong, J.; Chen, Q.; Gao, X.; Zhou, H. Manipulation of Facet Orientation in Hybrid Perovskite Polycrystalline Films by Cation Cascade. *Nat. Commun.* **2018**, *9*, 2793.

(14) Lv, Q.; He, W.; Lian, Z.; Ding, J.; Li, Q.; Yan, Q. Anisotropic Moisture Erosion of $CH_3NH_3PbI_3$ Single Crystals. *CrystEngComm* **2017**, *19*, 901−904.

(15) Venkatesan, N. R.; Labram, J. G.; Chabinyc, M. L. Charge-Carrier Dynamics and Crystalline Texture of Layered Ruddlesden−Popper Hybrid Lead Iodide Perovskite Thin Films. *ACS Energy Lett.* **2018**, *3*, 380−386.

(16) Chen, A. Z.; Shiu, M.; Ma, J. H.; Alpert, M. R.; Zhang, D.; Foley, B. J.; Smilgies, D.-M.; Lee, S.-H.; Choi, J. J. Origin of Vertical Orientation in Two-Dimensional Metal Halide Perovskites and Its Effect on Photovoltaic Performance. *Nat. Commun.* **2018**, *9*, 1336.

(17) Fu, W.; Wang, J.; Zuo, L.; Gao, K.; Liu, F.; Ginger, D. S.; Jen, A. K.-Y. Two-Dimensional Perovskite Solar Cells with 14.1% Power Conversion Efficiency and 0.68% External Radiative Efficiency. *ACS Energy Lett.* **2018**, *3*, 2086−2093.

(18) Giesbrecht, N.; Schlipf, J.; Grill, I.; Rieder, P.; Dyakonov, V.; Bein, T.; Hartschuh, A.; Müller-Buschbaum, P.; Docampo, P. Single-Crystal-like Optoelectronic-Properties of $MAPbI_3$ Perovskite Polycrystalline Thin Films. *J. Mater. Chem. A* **2018**, *6*, 4822−4828.

(19) Saliba, M.; Tan, K. W.; Sai, H.; Moore, D. T.; Scott, T.; Zhang, W.; Estroff, L. A.; Wiesner, U.; Snaith, H. J. Influence of Thermal Processing Protocol upon the Crystallization and Photovoltaic Performance of Organic−Inorganic Lead Trihalide Perovskites. *J. Phys. Chem. C* **2014**, *118*, 17171−17177.

(20) Ji, F.; Pang, S.; Zhang, L.; Zong, Y.; Cui, G.; Padture, N. P.; Zhou, Y. Simultaneous Evolution of Uniaxially Oriented Grains and Ultralow-Density Grain-Boundary Network in $CH_3NH_3PbI_3$ Perovskite Thin Films Mediated by Precursor Phase Metastability. *ACS Energy Lett.* **2017**, *2*, 2727−2733.

(21) Lee, D. S.; Yun, J. S.; Kim, J.; Soufiani, A. M.; Chen, S.; Cho, Y.; Deng, X.; Seidel, J.; Lim, S.; Huang, S.; Ho-Baillie, A. W. Y. Passivation of Grain Boundaries by Phenethylammonium in Formamidinium-Methylammonium Lead Halide Perovskite Solar Cells. *ACS Energy Lett.* **2018**, *3*, 647−654.

(22) Wang, Z.; Lin, Q.; Chmiel, F. P.; Sakai, N.; Herz, L. M.; Snaith, H. J. Efficient Ambient-Air-Stable Solar Cells with 2D−3D Heterostructured Butylammonium-Caesium-Formamidinium Lead Halide Perovskites. *Nat. Energy* **2017**, *2*, 17135.

(23) Zhao, T.; Liu, H.; Ziffer, M. E.; Rajagopal, A.; Zuo, L.; Ginger, D. S.; Li, X.; Jen, A. K. Y. Realization of a Highly Oriented $MAPbBr_3$ Perovskite Thin Film via Ion Exchange for Ultrahigh Color Purity Green Light Emission. *ACS Energy Lett.* **2018**, *3*, 1662−1669.

(24) Park, B.; Kedem, N.; Kulbak, M.; Lee, D. Y.; Yang, W. S.; Jeon, N. J.; Seo, J.; Kim, G.; Kim, K. J.; Shin, T. J.; Hodes, G.; Cahen, D.; Seok, S. I. Understanding How Excess Lead Iodide Precursor Improves Halide Perovskite Solar Cell Performance. *Nat. Commun.* **2018**, *9*, 3301.

(25) Chiang, C.-H.; Wu, C.-G. A Method for the Preparation of Highly Oriented $MAPbI_3$ Crystallites for High-Efficiency Perovskite Solar Cells to Achieve an 86% Fill Factor. *ACS Nano* **2018**, *12*, 10355−10364.

(26) Meng, L.; Sun, C.; Wang, R.; Huang, W.; Zhao, Z.; Sun, P.; Huang, T.; Xue, J.; Lee, J.-W.; Zhu, C.; Huang, Y.; Li, Y.; Yang, Y. Tailored Phase Conversion under Conjugated Polymer Enables Thermally Stable Perovskite Solar Cells with Efficiency Exceeding 21%. *J. Am. Chem. Soc.* **2018**, *140*, 17255−17262.

(27) Zhao, Y.; Tan, H.; Yuan, H.; Yang, Z.; Fan, J. Z.; Kim, J.; Voznyy, O.; Gong, X.; Quan, L. N.; Tan, C. S.; Hofkens, J.; Yu, D.; Zhao, Q.; Sargent, E. H. Perovskite Seeding Growth of Formamidinium-Lead-Iodide-Based Perovskites for Efficient and Stable Solar Cells. *Nat. Commun.* **2018**, *9*, 1607.

(28) Wang, Y.; Sun, X.; Chen, Z.; Sun, Y.-Y.; Zhang, S.; Lu, T.-M.; Wertz, E.; Shi, J. High-Temperature Ionic Epitaxy of Halide Perovskite Thin Film and the Hidden Carrier Dynamics. *Adv. Mater.* **2017**, *29*, 1702643.

(29) Chen, J.; Morrow, D. J.; Fu, Y.; Zheng, W.; Zhao, Y.; Dang, L.; Stolt, M. J.; Kohler, D. D.; Wang, X.; Czech, K. J.; Hautzinger, M. P.; Shen, S.; Guo, L.; Pan, A.; Wright, J. C.; Jin, S. Single-Crystal Thin Films of Cesium Lead Bromide Perovskite Epitaxially Grown on Metal Oxide Perovskite ($SrTiO_3$). *J. Am. Chem. Soc.* **2017**, *139*, 13525−13532.

(30) Christians, J. A.; Miranda Herrera, P. A.; Kamat, P. V. Transformation of the Excited State and Photovoltaic Efficiency of $CH_3NH_3PbI_3$ Perovskite upon Controlled Exposure to Humidified Air. *J. Am. Chem. Soc.* **2015**, *137*, 1530−1538.

(31) Celio, H. Interface Designed with Differential Pumping and Built-in Figure of Merit to Monitor Chambers Where Environ-

DOI: 10.1021/acsaem.9b01298
ACS Appl. Energy Mater. XXXX, XXX, XXX−XXX

mentally Sensitive Samples Are Prepared or Transferred for Analysis. 9,945,761 B2, April 17, 2018.
(32) Castle, J. E.; Chapman-Kpodo, H.; Proctor, A.; Salvi, A. M. Curve-Fitting in XPS Using Extrinsic and Intrinsic Background Structure. *J. Electron Spectrosc. Relat. Phenom.* **2000**, *106*, 65−80.
(33) Wang, Z.; Jin, K.; Zhang, Y.; Wang, F.; Zhu, Z. ToF-SIMS Depth Profiling of Insulating Samples, Interlaced Mode or Non-Interlaced Mode? *Surf. Interface Anal.* **2014**, *46*, 257−260.
(34) Jesper Jacobsson, T.; Correa-Baena, J.-P.; Pazoki, M.; Saliba, M.; Schenk, K.; Grätzel, M.; Hagfeldt, A. Exploration of the Compositional Space for Mixed Lead Halogen Perovskites for High Efficiency Solar Cells. *Energy Environ. Sci.* **2016**, *9*, 1706−1724.
(35) Shannon, R. D. Revised Effective Ionic Radii and Systematic Studies of Interatomic Distances in Halides and Chalcogenides. *Acta Crystallogr., Sect. A: Cryst. Phys., Diffr., Theor. Gen. Crystallogr.* **1976**, *32*, 751−767.
(36) Stoumpos, C. C.; Malliakas, C. D.; Kanatzidis, M. G. *Inorg. Chem.* **2013**, *52*, 9019−9038.
(37) Katari, J. E. B.; Colvin, V. L.; Alivisatos, A. P. X-Ray Photoelectron Spectroscopy of CdSe Nanocrystals with Applications to Studies of the Nanocrystal Surface. *J. Phys. Chem.* **1994**, *98*, 4109−4117.
(38) Murali, B.; Dey, S.; Abdelhady, A. L.; Peng, W.; Alarousu, E.; Kirmani, A. R.; Cho, N.; Sarmah, S. P.; Parida, M. R.; Saidaminov, M. I.; Zhumekenov, A. A.; Sun, J.; Alias, M. S.; Yengel, E.; Ooi, B. S.; Amassian, A.; Bakr, O. M.; Mohammed, O. F. Surface Restructuring of Hybrid Perovskite Crystals. *ACS Energy Lett.* **2016**, *1*, 1119−1126.
(39) Matteocci, F.; Busby, Y.; Pireaux, J.-J.; Divitini, G.; Cacovich, S.; Ducati, C.; Di Carlo, A. Interface and Composition Analysis on Perovskite Solar Cells. *ACS Appl. Mater. Interfaces* **2015**, *7*, 26176−26183.
(40) Griffin, M. P.; Gearba, R.; Stevenson, K. J.; Vanden Bout, D. A.; Dolocan, A. Revealing the Chemistry and Morphology of Buried Donor/Acceptor Interfaces in Organic Photovoltaics. *J. Phys. Chem. Lett.* **2017**, *8*, 2764.
(41) Siegler, T. D.; Shimpi, T. M.; Sampath, W. S.; Korgel, B. A. Development of Wide Bandgap Perovskites for Next-Generation Tandem Solar Cells. *Chem. Eng. Sci.* **2019**, *199*, 388−397.
(42) Wu, B.; Yuan, H.; Xu, Q.; Steele, J. A.; Giovanni, D.; Puech, P.; Fu, J.; Ng, Y. F.; Jamaludin, N. F.; Solanki, A.; Mhaisalkar, S.; Mathews, N.; Roeffaers, M. B. J.; Grätzel, M.; Hofkens, J.; Sum, T. C. Indirect Tail States Formation by Thermal-Induced Polar Fluctuations in Halide Perovskites. *Nat. Commun.* **2019**, *10*, 484.
(43) Lu, M.; Zhang, X.; Bai, X.; Wu, H.; Shen, X.; Zhang, Y.; Zhang, W.; Zheng, W.; Song, H.; Yu, W. W.; Rogach, A. L. Spontaneous Silver Doping and Surface Passivation of $CsPbI_3$ Perovskite Active Layer Enable Light-Emitting Devices with an External Quantum Efficiency of 11.2%. *ACS Energy Lett.* **2018**, *3*, 1571−1577.
(44) Chen, Q.; Chen, L.; Ye, F.; Zhao, T.; Tang, F.; Rajagopal, A.; Jiang, Z.; Jiang, S.; Jen, A. K.-Y.; Xie, Y.; Cai, J.; Chen, L. Ag-Incorporated Organic−Inorganic Perovskite Films and Planar Heterojunction Solar Cells. *Nano Lett.* **2017**, *17*, 3231−3237.
(45) Mahmoudi, T.; Wang, Y.; Hahn, Y.-B. Stability Enhancement in Perovskite Solar Cells with Perovskite/Silver−Graphene Composites in the Active Layer. *ACS Energy Lett.* **2019**, *4*, 235−241.
(46) Zhou, S.; Ma, Y.; Zhou, G.; Xu, X.; Qin, M.; Li, Y.; Hsu, Y.-J.; Hu, H.; Li, G.; Zhao, N.; Xu, J.; Lu, X. Ag-Doped Halide Perovskite Nanocrystals for Tunable Band Structure and Efficient Charge Transport. *ACS Energy Lett.* **2019**, *4*, 534−541.
(47) Kato, Y.; Ono, L. K.; Lee, M. V.; Wang, S.; Raga, S. R.; Qi, Y. Silver Iodide Formation in Methyl Ammonium Lead Iodide Perovskite Solar Cells with Silver Top Electrodes. *Adv. Mater. Interfaces* **2015**, *2*, 1500195.
(48) Guerrero, A.; You, J.; Aranda, C.; Kang, Y. S.; Garcia-Belmonte, G.; Zhou, H.; Bisquert, J.; Yang, Y. Interfacial Degradation of Planar Lead Halide Perovskite Solar Cells. *ACS Nano* **2016**, *10*, 218−224.
(49) Back, H.; Kim, G.; Kim, J.; Kong, J.; Kim, T. K.; Kang, H.; Kim, H.; Lee, J.; Lee, S.; Lee, K. Achieving Long-Term Stable Perovskite Solar Cells via Ion Neutralization. *Energy Environ. Sci.* **2016**, *9*, 1258−1263.
(50) Sanehira, E. M.; Tremolet de Villers, B. J.; Schulz, P.; Reese, M. O.; Ferrere, S.; Zhu, K.; Lin, L. Y.; Berry, J. J.; Luther, J. M. Influence of Electrode Interfaces on the Stability of Perovskite Solar Cells: Reduced Degradation Using MoO_x/Al for Hole Collection. *ACS Energy Lett.* **2016**, *1*, 38−45.
(51) Fransishyn, K. M.; Kundu, S.; Kelly, T. L. Elucidating the Failure Mechanisms of Perovskite Solar Cells in Humid Environments Using In Situ Grazing-Incidence Wide-Angle X-Ray Scattering. *ACS Energy Lett.* **2018**, *3*, 2127−2133.
(52) Liu, Z.; Krückemeier, L.; Krogmeier, B.; Klingebiel, B.; Márquez, J. A.; Levcenko, S.; Öz, S.; Mathur, S.; Rau, U.; Unold, T.; Kirchartz, T. Open-Circuit Voltages Exceeding 1.26 V in Planar Methylammonium Lead Iodide Perovskite Solar Cells. *ACS Energy Lett.* **2019**, *4*, 110−117.
(53) Wang, J.; Fu, W.; Jariwala, S.; Sinha, I.; Jen, A. K.-Y.; Ginger, D. S. Reducing Surface Recombination Velocities at the Electrical Contacts Will Improve Perovskite Photovoltaics. *ACS Energy Lett.* **2019**, *4*, 222−227.
(54) Qiao, H. W.; Yang, S.; Wang, Y.; Chen, X.; Wen, T. Y.; Tang, L. J.; Cheng, Q.; Hou, Y.; Zhao, H.; Yang, H. G. A Gradient Heterostructure Based on Tolerance Factor in High-Performance Perovskite Solar Cells with 0.84 Fill Factor. *Adv. Mater.* **2019**, *31*, 1804217.
(55) Srimath Kandada, A. R.; Neutzner, S.; D'Innocenzo, V.; Tassone, F.; Gandini, M.; Akkerman, Q. A.; Prato, M.; Manna, L.; Petrozza, A.; Lanzani, G. Nonlinear Carrier Interactions in Lead Halide Perovskites and the Role of Defects. *J. Am. Chem. Soc.* **2016**, *138*, 13604−13611.
(56) Zhang, M.; Zheng, Z.; Fu, Q.; Guo, P.; Zhang, S.; Chen, C.; Chen, H.; Wang, M.; Luo, W.; Tian, Y. Determination of Defect Levels in Melt-Grown All-Inorganic Perovskite $CsPbBr_3$ Crystals by Thermally Stimulated Current Spectra. *J. Phys. Chem. C* **2018**, *122*, 10309−10315.
(57) Stewart, R. J.; Grieco, C.; Larsen, A. V.; Doucette, G. S.; Asbury, J. B. Molecular Origins of Defects in Organohalide Perovskites and Their Influence on Charge Carrier Dynamics. *J. Phys. Chem. C* **2016**, *120*, 12392−12402.
(58) Winterbottom, W. L. Equilibrium Shape of a Small Particle in Contact with a Foreign Substrate. *Acta Metall.* **1967**, *15*, 303−310.
(59) Seifert, A.; Vojta, A.; Speck, J. S.; Lange, F. F. Microstructural Instability in Single-Crystal Thin Films. *J. Mater. Res.* **1996**, *11*, 1470−1482.
(60) Thompson, C. V. Structure Evolution During Processing of Polycrystalline Films. *Annu. Rev. Mater. Sci.* **2000**, *30*, 159−190.
(61) Ohring, M. *Material Science of Thin Films*, 2nd ed.; Academic Press: San Diego, CA, 2002.
(62) Weissbuch, I.; Guo, S.; Edgar, R.; Cohen, S.; Howes, P.; Kjaer, K.; Als-Nielsen, J.; Lahav, M.; Leiserowitz, L. Oriented Crystalline Thin Films of Tetracosanedioic Acid and Its Metal Salts at the Air-Aqueous Solution Interface. *Adv. Mater.* **1998**, *10*, 117−121.
(63) Tao, A. R.; Habas, S.; Yang, P. Shape Control of Colloidal Metal Nanocrystals. *Small* **2008**, *4*, 310−325.
(64) Cho, S. H.; Ghosh, S.; Berkson, Z. J.; Hachtel, J. A.; Shi, J.; Zhao, X.; Reimnitz, L. C.; Dahlman, C. J.; Ho, Y.; Yang, A.; Liu, Y.; Idrobo, J.-C.; Chmelka, B. F.; Milliron, D. J. Syntheses of Colloidal F:In_2O_3 Cubes: Fluorine-Induced Faceting and Infrared Plasmonic Response. *Chem. Mater.* **2019**, *31*, 2661−2676.
(65) Mao, C.; Zhou, L.; Wu, X.; Sun, X. New Understanding of Silver-Induced Texture in Powder-in-Tube Processed Ag/Bi(2223) Tape. *Phys. C* **1997**, *281*, 159−175.
(66) Luo, J. S.; Merchant, N.; Maroni, V. A.; Riley, G. N.; Carter, W. L. Influence of Silver Cladding on the Formation and Alignment of the $(Bi_{2-x}Pb_x)Sr_2Ca_2Cu_3O_{10+\delta}$ Phase. *Appl. Phys. Lett.* **1993**, *63*, 690−692.
(67) Aswal, D. K.; Gupta, S. K.; Debnath, A. K.; Kothiyal, G. P.; Sabharwal, S. C.; Gupta, M. K. Preparation of Adherent Y-Ba-Cu-O

DOI: 10.1021/acsaem.9b01298
ACS Appl. Energy Mater. XXXX, XXX, XXX−XXX

Thick Films and the Effect of Silver Doping. *Supercond. Sci. Technol.* **1991**, *4*, 188−191.
(68) Kim, F.; Connor, S.; Song, H.; Kuykendall, T.; Yang, P. Platonic Gold Nanocrystals. *Angew. Chem.* **2004**, *116*, 3759−3763.
(69) Liu, M.; Guyot-Sionnest, P. Mechanism of Silver(I)-Assisted Growth of Gold Nanorods and Bipyramids. *J. Phys. Chem. B* **2005**, *109*, 22192−22200.
(70) Lin, Y.; Fang, Y.; Zhao, J.; Shao, Y.; Stuard, S. J.; Nahid, M. M.; Ade, H.; Wang, Q.; Shield, J. E.; Zhou, N.; Moran, A. M.; Huang, J. Unveiling the Operation Mechanism of Layered Perovskite Solar Cells. *Nat. Commun.* **2019**, *10*, 1008.

DOI: 10.1021/acsaem.9b01298
ACS Appl. Energy Mater. XXXX, XXX, XXX−XXX